PHYSICAL REVIEW B **95**, 174405 (2017)

Electronic transport on the Shastry-Sutherland lattice in Ising-type rare-earth tetraborides

Linda Ye,* Takehito Suzuki, and Joseph G. Checkelsky
Department of Physics, Massachusetts Institute of Technology, Cambridge, Massachusetts 02139, USA
(Received 7 March 2017; revised manuscript received 14 April 2017; published 3 May 2017)

In the presence of a magnetic field frustrated spin systems may exhibit plateaus at fractional values of saturation magnetization. Such plateau states are stabilized by classical and quantum mechanisms including order by disorder, triplon crystallization, and various competing order effects. In the case of electrically conducting systems, free electrons represent an incisive probe for the plateau states. Here we study the electrical transport of Ising-type rare-earth tetraborides RB_4 (R = Er, Tm), a metallic Shastry-Sutherland lattice showing magnetization plateaus. We find that the longitudinal and transverse resistivities reflect scattering with both the static and the dynamic plateau structure. We model these results consistently with the expected strong uniaxial anisotropy on a quantitative level, providing a framework for the study of plateau states in metallic frustrated systems.

DOI: 10.1103/PhysRevB.95.174405

I. INTRODUCTION

Geometrically frustrated lattices play host to a number of emergent quantum mechanical phases including quantum spin liquids [1], resonating valence bond states [2], and complex magnetic orders [3]. Such systems are typically electronic insulators constructed from low-connectivity lattices that enforce competing magnetic interactions and enhanced quantum mechanical fluctuations [4]. While in many cases the introduction of charge carriers destabilizes such lattice-borne frustration, recently a variety of frustration-related effects have been discussed in this context in a class of materials termed frustrated metallic systems [5]. Examples include kagome lattice model realizations of the fractional quantum Hall effect [6] and superconductors with exotic pairing symmetries [7,8]. To what extent such phenomena can be realized in experiments is an open question.

A known materials system that has both lattice frustration and itinerant electronic behavior is the rare-earth (R) tetraboride RB_4. The system is tetragonal (space group $P4/mbm$) with magnetic R ions embedded in a boron network and forming a lattice topologically equivalent to the Shastry-Sutherland lattice (SSL) in the ab plane shown in Fig. 1(a). In the ab plane of the unit cell there are four R ions, located at ($0.318a$, $0.818a$), ($0.182a$, $0.318a$), ($0.818a$, $0.682a$) and ($0.682a$, $0.182a$), where a is the lattice parameter (the complete boron network is described elsewhere [9]). While the $4f$ electrons of the R ions are localized in a frustrated configuration, the $5d$ electrons from R and $2p$ from B act as itinerant carriers [9]. As with other SSL systems, the key parameters determining the frustration are the antiferromagnetic exchange J_1 and J_2 ($J_1, J_2 > 0$) on diagonal and square bonds on alternating tiles [10]. Unlike the celebrated case of quantum spin-1/2 Cu^{2+} ions in the insulating compound $SrCu_2(BO_3)_2$, which realizes the collective dimer singlet ground state predicted for the SSL [10,11], RB_4 has large classical f moments with magnetic interactions mediated by itinerant electrons. Despite this, just as $SrCu_2(BO_3)_2$ exhibits a series of fractional magnetization plateaus as a function of the magnetic field H with $M/M_S = 1/q$ (q here is an integer from 2 to 9, M is the magnetization, and M_S is the saturation M) [11–14], RB_4 also shows magnetization plateaus of unusual structure [15–18]. A particularly interesting limit is the trivalent R = Er and Tm, where a strong Ising single-ion anisotropy exists such that the f-electron moments may be described within up/down twofold degrees of freedom locked perpendicular to the SSL plane and the plateau transitions arise from complex spin-flip processes [19–22].

Herein we investigate how static and dynamic aspects of the magnetism in Ising-like RB_4 influence transport and the view it offers into the energetics of the classical SSL magnetic phase diagram. The SSL network for ErB_4 and TmB_4 along with their Ising-type antiferromagnetic (AFM) ground states are shown in Figs. 1(b) and 1(c), respectively [16,23]. The a and c lattice constants are 7.071 and 4.000 Å, respectively, for ErB_4 and 7.057 and 3.987 Å, respectively, for TmB_4. In both materials the magnetic structure repeats uniformly in layers along the c axis [9,18]. One view of the difference between the two systems is the connectivity of the spins: in ErB_4 the spins on the diagonal bonds are antiparallel, while in TmB_4 they are parallel. This can be understood in terms of exchange interactions, as while both compounds have $J_1 \approx J_2 > 0$, they differ in further neighbor interactions [16,21]. With $H \parallel c$, in ErB_4 the possible sites for field-dependent spin flips occur on one-dimensional (1D) ferromagnetic chains connected by J_2 that are decoupled unless a fourth neighbor interaction J_4 is included. For TmB_4 a third neighbor interaction J_3 complementary to J_1 allows instead for a 2D network of possible spin flips. These differences can be connected to the corresponding plateau structures, which are shown in Fig. 1(d). Common to both systems are plateaus at $M_S/2$, while TmB_4 shows an additional plateau with a higher denominator depending on the history and q may take noninteger values, as also shown in Fig. 1(d) [16]. As we discuss below, these differences in magnetism also have a significant impact on electronic transport.

II. METHODS

Single crystals of ErB_4 and TmB_4 were grown using the floating-zone method. We reacted 99.99% pure Er_2O_3 or 99.99% pure Tm_2O_3 with 99% pure B in Ar flow to form polycrystalline tetraborides [23], from which single

*lindaye@mit.edu

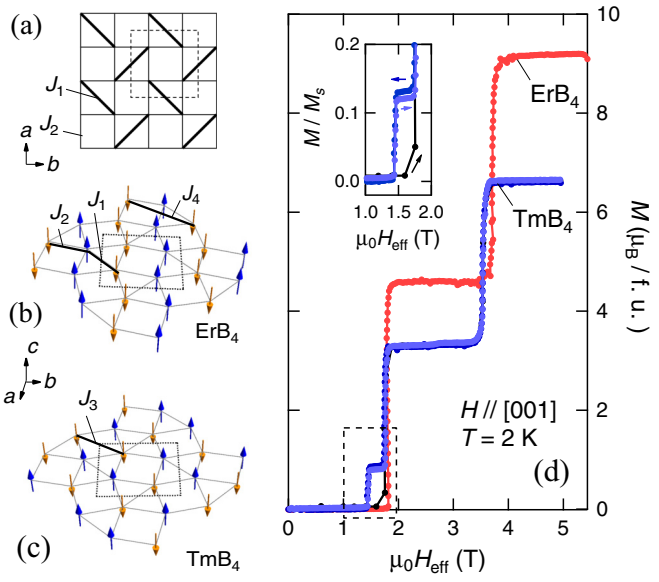

FIG. 1. Shastry-Sutherland lattice and magnetization plateaus in ErB_4 and TmB_4. (a) SSL model with diagonal bond J_1 and square bond J_2. (b, c) Spin configuration for antiferromagnetic ground states in ErB_4 and TmB_4, respectively. Exchange couplings J_1, J_2, J_3, and J_4 and the unit cell (dashed line) are shown. (d) Magnetization as a function of the field $\mu_0 H_{\rm eff}$ applied along the c axis for ErB_4 and TmB_4. Inset: Magnified view near the $(1/q)M_s$ phase in TmB_4. Light blue (dark blue) curves represent scans with an increasing (a decreasing) field between ± 5 T. The plateau values (defined at the midpoint of the plateau) for the two scan directions are 0.121 M_s ($q \simeq 8.3$) and 0.132 M_s ($q \simeq 7.6$), respectively.

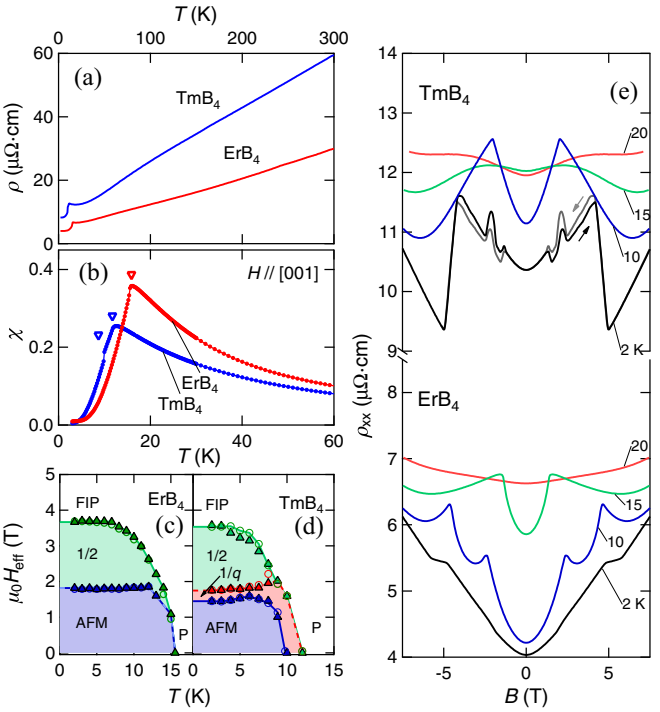

FIG. 2. Magnetic phase diagram of ErB_4 and TmB_4. (a) Resistivity ρ as a function of temperature T for the SSL plane of ErB_4 and TmB_4 single crystals. (b) Volume magnetic susceptibility χ measured along the c axis for ErB_4 and TmB_4. Triangles denote transition temperatures. (c, d) Phase diagram in the H-T plane for ErB_4 and (trained) TmB_4, respectively. The boundaries determined from transport are represented by triangles; those determined from magnetization, by circles. (e) Magnetic-field dependence of the longitudinal resistivity $\rho_{xx}(B)$ at selected T for TmB_4 and ErB_4.

crystals were obtained after further zone refining. Powder x-ray diffraction was done to confirm that the materials are of a single phase and single-crystal scattering was performed to orient crystals.

Measurements of M were performed using a commercial SQUID magnetometer with a field applied along the [001] tetragonal axis. The demagnetization factor N calculated from sample dimensions [24] and the measured M were used to obtain the effective field $H_{\rm eff} = H - NM$ and magnetic induction $B = \mu_0(H_{\rm eff} + M)$ for magnetization and transport measurements, respectively. Here μ_0 is the vacuum permeability. The contributions from R moments are significant, with $\mu_0 M_s = 2.14$ and 1.56 T for ErB_4 and TmB_4, respectively.

Electrical measurements were performed using a standard low-frequency (18.3-Hz) ac technique with a 2-mA excitation in a commercial cryostat. The magnetic field was applied along [001] as in magnetization measurements, with the current applied in the (001) Shastry-Sutherland plane. The dimensions of transport samples used here are $0.71\times0.33(ab)\times0.02(c)$ mm^3 (ErB_4) and $0.71\times0.28(ab)\times0.03(c)$ mm^3 (TmB_4). ρ_{xx} (ρ_{yx}) is obtained from symmetrization (antisymmetrization) between time-reversed processes.

III. RESULTS AND DISCUSSION

RB_4 are metals and the metallicity of ErB_4 and TmB_4 is similar. Starting with ErB_4, as shown in Fig. 2(a) the resistivity ρ as a function of T is metallic over the range $T = 2$ to 300 K. There is a kink in $\rho(T)$ observed at low T which corresponds to the AFM ordering temperature T_N as observed in the temperature dependence of the magnetic susceptibility $\chi(T)$ shown in Fig. 2(b). The response is distinct from the shoulderlike features observed for typical antiferromagnetic metals such as Cr and Dy [25], where the AFM ordering opens superzone gaps on the Fermi surface. Here this indicates an absence of Brillouin zone folding consistent with that the AFM magnetic unit cell is identical to the crystallographic unit cell. The field-temperature phase diagram is shown in Fig. 2(c); with increasing $\mu_0 H_{\rm eff}$ ErB_4 realizes a plateau state with $M_S/2$ and eventually enters a field-induced paramagnetic (FIP) phase (see also Fig. 1(d)). As shown in Fig. 2(e), below T_N a series of magnetoresistance features appears at the phase boundaries in Fig. 2(c). In particular, prominent peaks are observed at the magnetic transitions at moderate T but are suppressed at the lowest T, 2 K.

The overall behavior of TmB_4 is similar to that of ErB_4, but with an additional magnetic transition observed in $\rho(T)$ and $\chi(T)$ [Figs. 2(a) and 2(b), respectively], resulting in the phase diagram shown in Fig. 2(d). We denote the additional intermediate phase $1/q$, as the value of M in this region has been reported to be history dependent (q may take a value of 7, 9, or 11 [16]) and may not be precisely quantized [26]. Interestingly, this higher degree of complexity

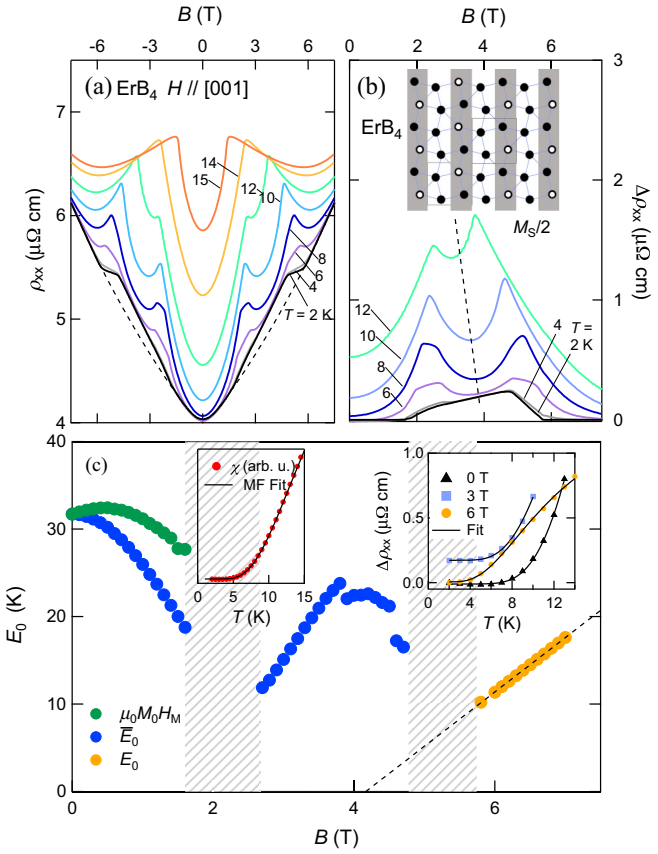

FIG. 3. Magnetic scattering in ErB_4. (a) Detailed magnetic-field dependence of the longitudinal resistivity $\rho_{xx}(B)$ of ErB_4 at $T < T_N$. (b) Magnetic contribution to resistivity $\Delta\rho_{xx}$ (see text). Inset: Possible configuration of the half-plateau state, with AFM stripes marked in gray. Here the black (white) circles represent spins parallel (antiparallel) to H. Dashed square frames enclose two types of unit cells for the $M_s/2$ phase. (c) Magnetic energy E_0 as a function of B. The hatched area represents regions with phase coexistence and the dashed line is a linear fit to the FIP phase. Left inset: Mean-field fitting to the magnetic susceptibility of ErB_4. Right inset: Fitting of $\Delta\rho_{xx}(T)$ at selected B.

is also reflected qualitatively in $\rho_{xx}(B)$. As shown in Fig. 2(e), a low-temperature hysteresis is observed in addition to sharp features corresponding to the magnetic transition.

A. Magnetoresistance in ErB_4

Detailed study of $\rho_{xx}(B)$ below T_N reveals connections to the magnetic phases and transitions in the Ising SSL system. We first focus on ErB_4 with $\rho_{xx}(B)$ shown in Fig. 3(a). The response can be understood as the sum of a conventional orbital magnetoresistance with additional scattering due to magnetic disorder and spin excitations as the plateau state evolves in field. To isolate the magnetic contribution, we calculate $\Delta\rho_{xx}(B,T) \equiv \rho_{xx}(B,T) - \rho^N_{xx}(B,2\text{ K})$, where we approximate the nonmagnetic contribution $\rho^N_{xx}(B,2\text{ K})$ [dashed line in Fig. 3(a)] as a second-order polynomial fit to the AFM and FIP phases, where M is constant at low T. As shown in Fig. 3(b), $\Delta\rho_{xx}$ exhibits a series of peaks at elevated T and a residual enhancement at intermediate B.

Unlike B-induced changes in resistivity for ρ^N_{xx} due to the Lorentz force, those in $\Delta\rho_{xx}$ arise from interaction of carriers with the magnetic state and therefore reflect a change in carrier relaxation time τ. The coexisting f moments and conduction electrons interact via a contact exchange interaction $\mathcal{H}_{cf} = J_{\text{c-f}}\boldsymbol{s}\cdot\boldsymbol{S}$, where $\boldsymbol{s}$ is the conduction electron spin and $\boldsymbol{S}$ is the total spin of localized magnetic moments [25,27]. It has been proposed that the $M_S/2$ state is comprised of alternating AFM and ferromagnetic stripes [see the inset in Fig. 3(b)] where a large degeneracy of ordering of the AFM stripes exists [21]. Such an additional degree of freedom can be expected to increase irregularities in the spin structure and therefore also in the periodic potential seen by the charge carriers causing increased scattering. This is consistent with the steplike rise seen in both the raw $\rho_{xx}(B)$ trace and the $\Delta\rho_{xx}(B)$ peak in the $M_S/2$ phase.

The pattern at elevated T in Fig. 3(b) suggests thermally enhanced magnetic scattering. For antiferromagnets in the strong Ising limit (where the exchange energy is less than the anisotropy energy), the lowest magnetic excitations are spin flips, as classical spin waves cost considerable anisotropy energies. In this context, the T excitation of the spin flips causes an increase in the spin-disorder resistivity (see Appendix) in the form [28,29]

$$\rho_m(T) \sim \text{sech}^2(E_0/k_BT), \tag{1}$$

where E_0 represents the magnetic energy at each site and k_B is the Boltzmann constant. At $B = 0$, E_0 equals $\mu_0 M_0 H_M$, with M_0 the rare-earth magnetic moment and H_M the effective molecular field at each site, and we get $E_0 = 32$ K from fitting $\Delta\rho_{xx}(T)$ with Eq. (1). This is comparable to the $E_0 = 23$ K obtained from the mean-field fitting to the magnetic susceptibility of the Ising moments in ErB_4 [30] [fit shown in Fig. 3(c), left inset],

$$\chi(T) = \frac{1 - m^2(T)}{T + E_0(1 - m^2(T))} + \chi_0, \tag{2}$$

where $m(T)$ stands for the solution of sublattice magnetization at each T to $m(T) = \tanh[E_0 m(T)/T]$. χ_0 represents the residual susceptibility, which is rarely T dependent.

Equation (1) may be further modified to describe the effects of finite fields taking $E_0 = \mu_0 M_0 |H_M \pm H_{\text{eff}}|$ and the sign depends on whether the magnetic moments align or antialign with the applied magnetic field. The green circles in Fig. 3(c) show the fit results of $\mu_0 M_0 H_M$ taking half of all spins to be parallel and half antiparallel to H_{eff}, where $\mu_0 M_0 H_M$ depends weakly on B within 30 ± 5 K. Alternatively, we show the average $\overline{E}_0$ obtained by assuming a single uniform E_0 using blue circles, and the evolution of $\overline{E}_0$ with B is shown in Fig. 3(c), with representative fits to Eq. (1) shown in the inset. As B is increased and the magnetic state is destabilized we see a drop in $\overline{E}_0$ from the zero-field value, 32 K. At the magnetic transitions [regions corresponding to transitions in $M(H_{\text{eff}})$ shown as hatched areas in Fig. 3(c)] a mixed magnetic phase is likely to exist and not be captured by the present model [31]. Upon entering the $M_S/2$ phase we see a rise in $\overline{E}_0$ to approximately 25 K, where the state is most stable, before it decreases again as the system approaches the transition to the FIP.

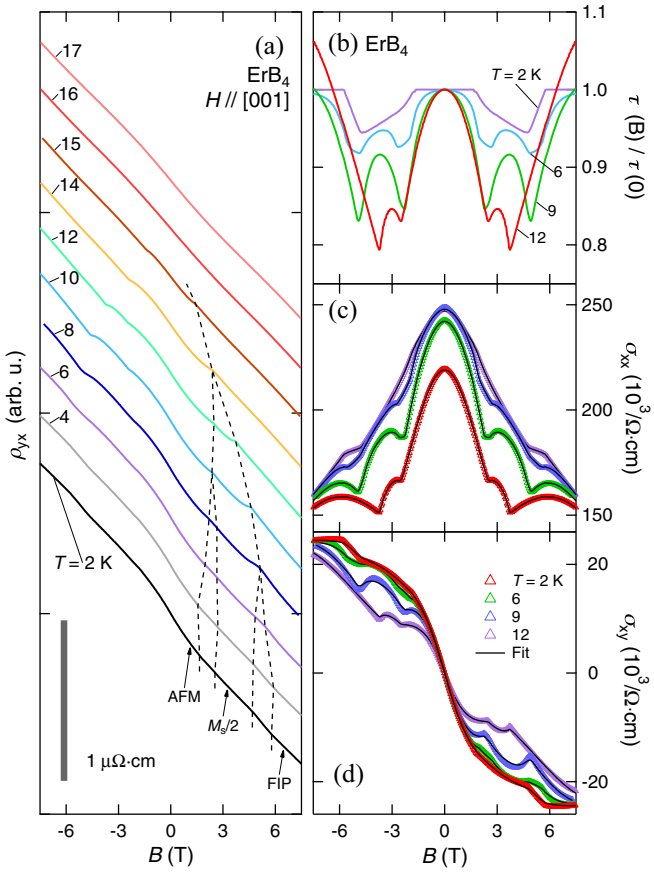

FIG. 4. Hall effect in ErB_4. (a) Field dependence of the transverse resistivity $\rho_{yx}(B)$ for ErB_4. Dashed lines represent the singularities observed in ρ_{xx}. (b) Relative relaxation time $\tau(B)/\tau_0$ as a function of B. (c) Longitudinal conductivity σ_{xx} and (d) transverse conductivity σ_{xy} fit with the modified two-band model using $\tau(B)/\tau_0$ [Eqs. (3) and (4)]. The legend is the same for both panels.

In the FIP phase, all the magnetic moments are uniformly aligned with B and $E_0 = \mu_0 M_0(H_{\text{eff}} - H_{\text{M}})$, with the Zeeman energy gain associated with the applied field overwhelming the AFM interactions. Here we expect a linear B dependence of E_0 as observed for fit results in the FIP phase [orange circles in Fig. 3(c)]. The slope yields $M_0 = 9.24\mu_B$, quantitatively consistent with the magnetic moment of Er^{3+} ($M_s = 9.6\mu_B$/Er). The positive intercept on B implies that the underlying interaction of the system is antiferromagnetic, and the FIP phase is destabilized at magnetic fields below 4 T.

B. Hall resistivity of ErB_4

We next examine the transverse resistivity ρ_{yx}. As shown in Fig. 4(a), there is an overall electronlike response, with weak kinks appearing as a function of B. The magnetic phase boundaries from the phase diagram in Fig. 2(c) are shown as dashed lines and closely track the features in ρ_{yx}. These features can be understood by the magnetic modifications to τ introduced above for ρ_{xx}. We employ a modified two-band model incorporating a field-dependent relaxation time $\tau(B)$

TABLE I. Fitting parameters for the two-band model for ErB_4. Sample A was measured between ±9 T; sample B, between ±18 T.

	n_1 (/cm^3)	μ_1 (cm^2/V·s)	n_2 (/cm^3)	μ_2 (cm^2/V·s)
Sample A				
σ_{xx}	1.74×10^{21}	716.9	8.15×10^{19}	3680.5
σ_{xy}	3.17×10^{20}	1218	1.816×10^{19}	4036
Sample B				
σ_{xx}	1.26×10^{21}	484.3	2.04×10^{20}	2064
σ_{xy}	2.2×10^{20}	1186	1.83×10^{19}	4441.7

for the longitudinal conductivity σ_{xx},

$$\sigma_{xx} = \sum_i \sigma^i_{xx} = \sum_i \frac{n_i e \mu_i (\tau(B)/\tau_0)}{1 + (\mu_i B)^2 (\tau(B)/\tau_0)^2}, \tag{3}$$

where σ^i_{xx}, n_i, and μ_i are the conductivity, carrier density, and mobility of each band, and τ_0 is the zero-field relaxation time at a given T. The total transverse conductivity σ_{xy} is written as

$$\sigma_{xy} = \sum_i \sigma^i_{xx} \cdot (\mu_i B) \cdot (\tau(B)/\tau_0). \tag{4}$$

The ratio $\tau(B)/\tau_0$ shown in Fig. 4(b) is obtained from $\Delta\rho_{xx}$, *viz*, $\tau(B)/\tau(0) = \rho_{xx}(0,T)/[\Delta\rho_{xx}(B,T) + \rho_{xx}(B,2\text{ K})]$.

As shown in Figs. 4(c) and 4(d), Eqs. (3) and (4) provide satisfactory fits for σ_{xx} and σ_{xy}, respectively. The best fits for σ_{xx} and σ_{xy} at $T = 2$ K are listed in Table I (also for a second sample, B). The set of parameters is similar for both fits, though there is a factor of 4–5 difference in carrier densities that optimize the longitudinal and transverse fits. We hypothesize that the lack of convergence is related to the Fermi surface's being composed of more than two bands [9]. However, higher order fitting is not a satisfactory proof of this, given the large number of parameters it introduces.

More generally, we suggest that this demonstrates that the features in ρ_{yx} may be captured by a field-induced scattering rate without showing clear signatures of the anomalous Hall effect conventionally observed in ferromagnets as a Hall effect proportional to M [32]. We point out that the magnitude of anomalous Hall conductivity σ^A_{xy} expected for the current system from the scaling relation between σ^A_{xy} and σ_{xx} is of the order 10^3 /Ω · cm [33], which is difficult to decompose unambiguously from the background Hall conductivities with prominent features upon magnetic phase transitions [see black fit curves in Fig. 4(d)]. We suggest that systems with reduced background σ_{xy} from the normal Hall conductivity σ^N_{xy} may provide a clearer view of the extrinsic/intrinsic anomalous Hall contributions in magnetization plateau systems. As $\sigma^N_{xy} \sim \tau$, this may be achieved by doping the boron sites in RB_4 with nonmagnetic elements to suppress τ while minimizing the influence on the magnetic subsystem. Low carrier compounds are also favorable as they possess a smaller σ^N_{xy} background, though care must be taken as small carrier systems may exist under a different physical regime in the universal scaling [33].

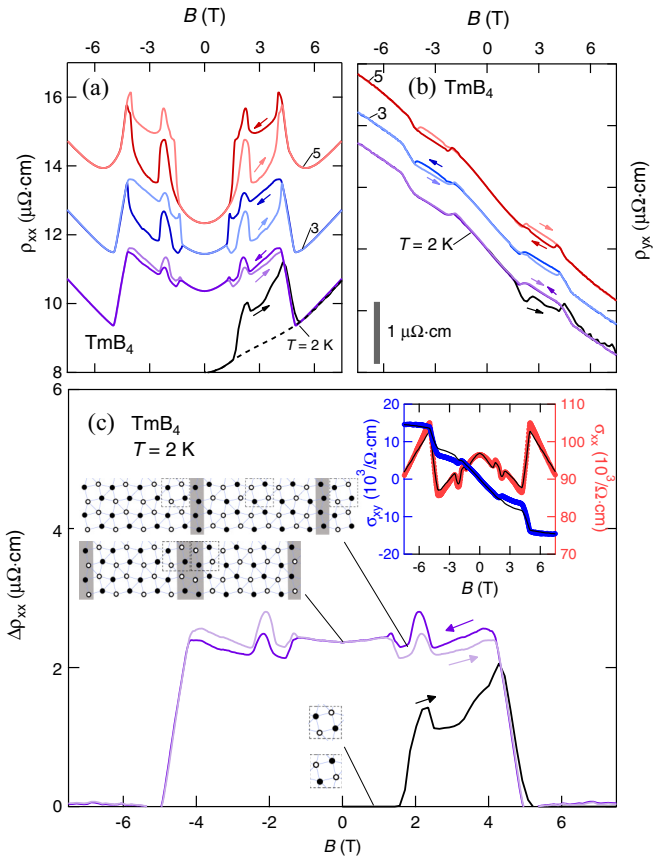

FIG. 5. Magnetotransport in TmB_4. (a) Longitudinal resistivity ρ_{xx} for TmB_4 at low T. The $T = 3$ K and $T = 5$ K curves are offset for clarity. (b) Transverse resistivity of TmB_4 at low T. (c) Magnetic contribution to resistivity $\Delta\rho_{xx}$ and possible magnetic configurations [16,26]. Inset: σ_{xx} and σ_{xy} fit with Eqs. (3) and (4). For clarity, only scans from negative to positive B are shown.

C. Transport in TmB_4

Turning to the detailed magnetotransport of TmB_4, the low-T behavior of ρ_{xx} and ρ_{yx} is shown in Figs. 5(a) and 5(b), respectively. Unlike the case of ErB_4, we observe hysteresis in both transport channels (also recently reported in another study [34]). Here hysteresis refers to the difference between time-reversed full-field sweeps. As shown in Fig. 1(d) hysteresis is observed in $M(H)$ in the vicinity of the $(1/q)M_s$ phase; in transport hysteresis appears across a B range corresponding approximately to both the $(1/q)M_s$ and the $M_s/2$ phases. Additionally, for ρ_{xx} we observe a difference between the zero-field cooled (virgin) state and the trained state (that seen after once reaching the FIP phase).

To probe the origin of these effects, we construct $\Delta\rho_{xx}$ in a manner analogous to that for ErB_4. In this case the normal component ρ_{xx}^N, which connects the AFM and FIP states, appears to belong to the virgin state, as shown by the dashed line in Fig. 5(a). Subtraction of this component yields $\Delta\rho_{xx}$ as shown in Fig. 5(c). The presence of additional scattering is evident in the trained phase. We note that this is contrary to the case of conventional domain wall scattering in ferromagnets, in which the virgin state typically has a higher resistivity [24].

TABLE II. Fitting parameters for the two-band model for TmB_4 (scan with increasing B).

	n_1 (/cm^3)	μ_1 (cm^2/V·s)	n_2 (/cm^3)	μ_2 (cm^2/V·s)
σ_{xx}	1.12×10^{21}	624	3.95×10^{18}	10467
σ_{xy}	6.8×10^{19}	1024	8.12×10^{19}	1063

Considerations of the detailed real-space magnetic textures resulting from the 2D spin flip network in this system offer insight into this unusual behavior and, more broadly, the appearance of the $(1/q)M_s$ phase [26]. The spin configuration for the zero-field cooled AFM state is known to have a magnetic unit cell identical to that of the crystallographic unit cell, as shown in Fig. 5(c) [16]. Starting from this simple AFM phase, with increasing B the $M_s/2$ phase and then the FIP phase are stabilized. The subsequent decrease in B to 0 realizes a cascade of phases with $M = M_s/2$, $(1/q)M_s$, and 0. However, the latter states are known to have larger real-space magnetic structures, which are evidently nearly degenerate in energy and accessible along this thermodynamic path [16,26]. One example of the expected long-period structure at $M = 0$ is shown in Fig. 5(c), with AFM domains in an antiphase periodic structure. It has been suggested that the alignment/shift of those AFM domains every 4/5 unit cells leads to the $(1/q)M_s$ phase in TmB_4 [26]. This characteristic of training and complexity is a hallmark of strong magnetic frustration in TmB_4; the resulting increase in ρ_{xx} can then be viewed as being due to domain wall scattering or the opening of superzone gaps in the Fermi surface if such structures are macroscopically ordered. In contrast, time-reversal antisymmetric quantities M and ρ_{yx} do not show training.

Similarly to the case of ErB_4, the patterns observed in both ρ_{xx} and ρ_{yx} for TmB_4 can largely be explained by the magnetic structure-sensitive changes in τ and spin disorder in the plateau phases. The fitting of σ_{xx} and σ_{xy} using Eqs. (3) and (4) is shown in the inset in Fig. 5(c) (parameters are listed in Table II). Fitting of the transport reproduces the experimental curves apart from in the $M_s/2$ phase. As deviations in the Hall response in magnetic systems are often due to the anomalous Hall effect, we suggest that this may be due to a skew scattering contribution from the ferromagnetically aligned domain walls [16,26]. In terms of modeling as employed in ErB_4, analysis of $\rho_{xx}(T)$ in the FIP phase yields a magnetic moment of $6.84\mu_B$ ($M_s = 6.66\mu_B$/Tm), molecular field of 1.74 T, and corresponding exchange energy of -0.69 meV. Here again transport offers a quantitative measure of the underling energy scales for the SSL.

IV. CONCLUSION

The present study demonstrates that transport is a sensitive probe of magnetic disorder and excitations in model metallic frustrated systems. In particular, the magnetotransport processes are found to be sensitive to static and dynamic magnetic disorder across plateau transitions and allow for quantitative characterization of the underlying magnetic order and its excitations. These results are consistent with the strong Ising anisotropy expected for $R =$ Er and Tm. Generally,

the enhancement in resistivity observed at the intermediate plateau phases favors a partially disordered state [21] or an additional number of domain walls [16,26] rather than uniform structures, examples of which have been proposed previously [20]. The results provide a framework in which to study the more complex RB_4 magnetization plateau series such as TbB_4 [17] and HoB_4 [18] with non-Ising-type anisotropies. More broadly, our study offers a new approach to a central question in frustrated magnetic systems, i.e., the nature of their elementary excitations. Yb_2Pt_2Pb is a metal recently identified as an anomalous quasi-1D quantum magnet in which electronic transport may be a probe of spinon dynamics [35]. Further application to systems with novel excitations such as monopoles in spin ice [36], spinons in spin liquids [37], and quasi-1D quantum magnets [38] could offer new insights into these phenomena.

ACKNOWLEDGMENTS

We are grateful to T. Senthil, I. Sodemann, and T. Kurumaji for fruitful discussions. This research was funded in part by the Gordon and Betty Moore Foundation EPiQS Initiative, Grant GBMF3848 to J.G.C. A portion of this work was performed at the National High Magnetic Field Laboratory, which is supported by National Science Foundation Cooperative Agreement No. DMR-1157490 and the State of Florida. L.Y. acknowledges support by the STC Center for Integrated Quantum Materials, NSF Grant No. DMR-1231319, and the Tsinghua Education Foundation.

APPENDIX

1. Resistivity analysis in ErB_4

We attribute the T evolution of ρ_{xx} to the inelastic scattering of conduction electrons by the magnetic subsystem. Due to the strong Ising anisotropy, the local moments can be adequately viewed as individual two-level systems split by molecular exchange fields. The level splitting is given by $2E_0 = 2\mu_0 H_1 M_0$.

The contribution to resistivity from inelastic scattering on localized quantum levels can be modeled as (following the description of crystal-field scattering [28])

$$\rho \sim \frac{1}{\tau} \sim |J_{\text{c-f}}|^2 \sum_{i,i'} |\langle m_s', i'|\boldsymbol{s}\cdot\boldsymbol{S}|m_s, i\rangle|^2 p_i f_{ii'}, \tag{A1}$$

where i and i' (m_s and m_s') denote the initial and final states of the magnetic moments (conduction electron spin), respectively. We define the occupation probability of the ith level as p_i and the Fermi factor as $f_{ii'}$, where

$$p_i = \frac{e^{-E_i/k_BT}}{\sum_j e^{-E_j/k_BT}}, \quad f_{ii'} = \frac{2}{1+e^{(E_{i'}-E_i)/k_BT}}. \tag{A2}$$

Here E_i and $E_{i'}$ are the energy of the localized moments before and after the scattering event, respectively.

Using $\pm$ to denote the two local levels with energies $\pm E_0$ we get

$$p_\pm = \frac{e^{\mp E_0/k_BT}}{e^{E_0/k_BT}+e^{-E_0/k_BT}}, \tag{A3}$$

and the Fermi factor raising (lowering) the energy of the magnetic system is

$$f_{\mp,\pm} = \frac{2}{1+e^{\pm 2E_0/k_BT}} = \frac{2}{e^{\pm E_0/k_BT}(e^{E_0/k_BT}+e^{-E_0/k_BT})}. \tag{A4}$$

Substituting Eq. (A3) and Eq. (A4) into Eq. (A1) we obtain the T dependence of ρ as

$$\rho \sim \text{sech}^2(E_0/k_BT). \tag{A5}$$

2. Parameters for two-band fitting

For ErB_4 we fit Eqs. (3) and (4) to σ_{xx} and σ_{xy} of two samples, A and B, respectively. In Table I we show the fitting parameters for sample A at 2 K up to 9 T and for sample B at 1.6 K up to 18 T. In each case there exist two electron bands with a relatively high (low) density and low (high) mobility.

For TmB_4, to avoid complications of the observed hysteresis we fit the negative-to-positive field scan with the resulting parameters listed in Table II. Similarly, two electronlike bands contribute to the conductivity.

[1] L. Balents, Spin liquids in frustrated magnets, Nature **464**, 199 (2010).
[2] P. W. Anderson, Resonating valence bonds: A new kind of insulator? Mater. Res. Bull. **8**, 153 (1973).
[3] J. E. Greedan, Geometrically frustrated magnetic materials, J. Mater. Chem. **11**, 37 (2001).
[4] A. P. Ramirez, Strongly geometrically frustrated magnets, Annu. Rev. Mater. Sci. **24**, 453 (1994).
[5] C. Lacroix, Frustrated metallic systems: A review of some peculiar behavior, J. Phys. Soc. Jpn. **79**, 011008 (2010).
[6] E. Tang, J.-W. Mei, and X.-G. Wen, High-Temperature Fractional Quantum Hall States, Phys. Rev. Lett. **106**, 236802 (2011).
[7] B.-J. Yang, Y. B. Kim, J. Yu, and K. Park, Doped valence-bond solid and superconductivity on the Shastry-Sutherland lattice, Phys. Rev. B **77**, 104507 (2008).
[8] J. Liu, N. Trivedi, Y. Lee, B. N. Harmon, and J. Schmalian, Quantum Phases in a Doped Mott Insulator on the Shastry-Sutherland Lattice, Phys. Rev. Lett. **99**, 227003 (2007).
[9] Z. P. Yin and W. E. Pickett, Rare-earth-boron bonding and $4f$ states in RB_4 tetraborides, Phys. Rev. B **77**, 035135 (2008).
[10] B. S. Shastry and B. Sutherland, Exact ground state of a quantum mechanical antiferromagnet, Physica B+C **108**, 1069 (1981).
[11] H. Kageyama, K. Yoshimura, R. Stern, N. V. Mushnikov, K. Onizuka, M. Kato, K. Kosuge, C. P. Slichter, T. Goto, and Y. Ueda, Exact Dimer Ground State and Quantized Magnetization Plateaus in the Two-Dimensional Spin System $SrCu_2(BO_3)_2$, Phys. Rev. Lett. **82**, 3168 (1999).
[12] K. Kodama, M. Takigawa, M. Horvatić, C. Berthier, H. Kageyama, Y. Ueda, S. Miyahara, F. Becca, and F. Mila,

Magnetic superstructure in the two-dimensional quantum antiferromagnet $SrCu_2(BO_3)_2$, Science **298**, 395 (2002).

[13] M. Takigawa, S. Matsubara, M. Horvatić, C. Berthier, H. Kageyama, and Y. Ueda, NMR Evidence for the Persistence of a Spin Superlattice Beyond the 1/8 Magnetization Plateau in $SrCu_2(BO_3)_2$, Phys. Rev. Lett. **101**, 037202 (2008).

[14] S. E. Sebastian, N. Harrison, P. Sengupta, C. D. Batista, S. Francoual, E. Palm, T. Murphy, N. Marcano, H. A. Dabkowska, and B. D. Gaulin, Fractalization drives crystalline states in a frustrated spin system, Proc. Natl. Acad. Sci. USA **105**, 20157 (2008).

[15] S. Michimura, A. Shigekawa, F. Iga, M. Sera, T. Takabatake, K. Ohoyama, and Y. Okabe, Magnetic frustrations in the Shastry-Sutherland system ErB_4, Physica B **378-380**, 596 (2006).

[16] K. Siemensmeyer, E. Wulf, H.-J. Mikeska, K. Flachbart, S. Gabáni, S. Matasš, P. Priputen, A. Efdokimova, and N. Shitsevalova, Fractional Magnetization Plateaus and Magnetic Order in the Shastry-Sutherland Magnet TmB_4, Phys. Rev. Lett. **101**, 177201 (2008).

[17] S. Yoshii, T. Yamamoto, M. Hagiwara, S. Michimura, A. Shigekawa, F. Iga, T. Takabatake, and K. Kindo, Multistep Magnetization Plateaus in the Shastry-Sutherland System TbB_4, Phys. Rev. Lett. **101**, 087202 (2008).

[18] S. Mat'asš, K. Siemensmeyer, E. Wheeler, E. Wulf, R. Beyer, Th. Hermannsdörfer, O. Ignatchik, M. Uhlarz, K. Flachbart, S. Gabáni, P. Priputen, A. Efdokimova, and N. Shitsevalova, Magnetism of rare earth tetraborides, J. Phys.: Conf. Ser. **200**, 032041 (2010).

[19] Y. I. Dublenych, Ground States of the Ising Model on the Shastry-Sutherland Lattice and the Origin of the Fractional Magnetization Plateaus in Rare-Earth-Metal Tetraborides, Phys. Rev. Lett. **109**, 167202 (2012).

[20] Y. I. Dublenych, Ground states of an Ising model on an extended Shastry-Sutherland lattice and the 1/2-magnetization plateau in some rare-earth-metal tetraborides, Phys. Rev. E **88**, 022111 (2013).

[21] K. Wierschem and P. Sengupta, Columnar Antiferromagnetic Order and Spin Supersolid Phase on the Extended Shastry-Sutherland Lattice, Phys. Rev. Lett. **110**, 207207 (2013).

[22] S. Michimura, A. Shigekawa, F. Iga, T. Takabatake, and K. Ohoyama, Complex magnetic structures of a Shastry-Sutherland lattice TmB_4 studied by powder neutron diffraction analysis, J. Phys. Soc. Jpn. **78**, 024707 (2009).

[23] J. Etourneau, J. P. Mercurio, A. Berrada, and P. Hagenmuller, The magnetic and electrical properties of some rare earth tetraborides, J. Less. Common Metal. **67**, 531 (1979).

[24] S. Chikazumi, *Physics of Ferromagnetism* (Oxford University Press, Oxford, UK, 1997).

[25] G. T. Meaden, Conduction electron scattering and the resistance of the magnetic elements, Contemp. Phys. **12**, 313 (1971).

[26] K. Wierschem, S. S. Sunku, T. Kong, T. Ito, P. C. Canfield, C. Panagopoulos, and P. Sengupta, Origin of modulated phases and magnetic hysteresis in TmB_4, Phys. Rev. B **92**, 214433 (2015).

[27] R. J. Elliot, *Magnetic Properties of Rare Earth Metals* (Springer, New York, 1972).

[28] V. U. S. Rao and W. E. Wallace, Calculation of the influence of the crystalline electric field on the spin-disorder resistivity of rare-earth alloys and comparison with results on $CeAl_2$, Phys. Rev. B **2**, 4613 (1970).

[29] T. Toliński, A. Kowalczyk, and V. Ivanov, Electrical resistivity of RNi_4B compounds (R = Y or rare earth), Phys. Stat. Sol. (b) **240**, 153 (2003).

[30] J. H. van Vleck, On the theory of antiferromagnetism, J. Chem. Phys. **9**, 85 (1941).

[31] J. F. Dillon, Jr., E. Y. Chen, and H. J. Guggenheim, Optical studies of the magnetic phase diagram of $FeCl_2$, Phys. Rev. B **18**, 377 (1978).

[32] N. Nagaosa, J. Sinova, S. Onoda, A. H. MacDonald, and N. P. Ong, Anomalous Hall effect, Rev. Mod. Phys. **82**, 1539 (2010).

[33] S. Onoda, N. Sugimoto, and N. Nagaosa, Quantum transport theory of anomalous electric, thermoelectric, and thermal Hall effects in ferromagnets, Phys. Rev. B **77**, 165103 (2008).

[34] S. S. Sunku, T. Kong, T. Ito, P. C. Canfield, B. S. Shastry, P. Sengupta, and C. Panagopoulos, Hysteretic magnetoresistance and unconventional anomalous Hall effect in the frustrated magnet TmB_4, Phys. Rev. B **93**, 174408 (2016).

[35] L. S. Wu, W. J. Gannon, I. A. Zaliznyak, A. M. Tsvelik, M. Brockmann, J.-S. Caux, M. S. Kim, Y. Qiu, J. R. D. Copley, G. Ehlers, A. Podlesnyak, and M. C. Aronson, Orbital-exchange and fractional quantum number excitations in an f-electron metal, Yb_2Pt_2Pb, Science **352**, 1206 (2016).

[36] C. Castelnovo, R. Moessner, and S. L. Sondhi, Magnetic monopoles in spin ice, Nature **451**, 42 (2008).

[37] T.-H. Han, J. S. Helton, S. Chu, D. G. Nocera, J. A. Rodriguez-Rivera, C. Broholm, and Y. S. Lee, Fractionalized excitations in the spin-liquid state of a kagome-lattice antiferromagnet, Nature **492**, 406 (2012).

[38] D. A. Tennant, T. G. Perring, R. A. Cowley, and S. E. Nagler, Unbound Spinons in the $S = 1/2$ Antiferromagnetic Chain $KCuF_3$, Phys. Rev. Lett. **70**, 4003 (1993).